

SOLUTION-ADAPTIVE MAGNETOHYDRODYNAMICS FOR SPACE PLASMAS: SUN-TO-EARTH SIMULATIONS

Space-environment simulations, particularly those involving space plasma, present significant computational challenges. Global computational models based on magnetohydrodynamics equations are essential to understanding the solar system's plasma phenomena, including the large-scale solar corona, the solar wind's interaction with planetary magnetospheres, comets, and interstellar medium, and the initiation, structure, and evolution of solar eruptive events.

Numerical simulation and modeling are increasingly essential to basic and applied space-physics research for two primary reasons. First, the heliosphere and magnetosphere are vast regions of space from which we have relatively few in situ measurements. Numerical simulations let us “stitch together” observations from different regions and provide data-interpretation insight to help us understand this complex system's global behavior. Second, models have evolved to where their physical content and numerical robustness, flexibility, and improving ease of use inspire researchers to apply them to intriguing scenarios with new measures of confidence.

Indeed, many shortcomings and questions remain for even the most advanced models in terms of inclusion of important physical mechanisms, the spatial and temporal domains they can address, and thorny technical numerical issues to be dispatched. Nonetheless, over the last several years modeling has crossed a threshold, making the transition from the arcane preserves of specialists to practical tools with widespread applications.

Global computational models based on first-principles mathematical physics descriptions are essential to understanding the solar system's plasma phenomena, including the large-scale solar corona, the solar wind's interaction with planetary magnetospheres, comets, and interstellar medium, and the initiation, structure, and evolution of solar eruptive events. Today, and for the foreseeable future, numerical models based on magnetohydrodynamics (MHD) equations are the only self-consistent mathematical descriptions that can span the enormous distances associated with large-scale space phenomena. Although providing only a relatively low-order approximation to actual plasma behavior, MHD models have successfully simulated many important space-plasma processes and provide a powerful means for significantly advancing process understanding.

Space scientists have used global MHD simula-

1521-9615/04/\$20.00 © 2004 IEEE
Copublished by the IEEE CS and the AIP

TAMAS I. GOMBOSI, KENNETH G. POWELL, DARREN L. DE ZEEUW, C. ROBERT CLAUER, KENNETH C. HANSEN, WARD B. MANCHESTER, AARON J. RIDLEY, ILIA I. ROUSSEV, IGOR V. SOKOLOV, AND QUENTIN F. STOUT,

University of Michigan

GÁBOR TÓTH

University of Michigan and Eötvös University, Budapest, Hungary

tions for over 25 years to simulate space plasmas. Early global-scale 3D MHD simulations focused on simulating the solar wind–magnetosphere system. Since then, researchers have used MHD models to study a range of solar system plasma environments. During the past 25 years, global MHD model numerical approaches have evolved in several ways. Early models were based on relatively simple central differencing methods, in which physical quantities are expressed as centered finite differences. Later models take advantage of the so-called high-resolution approach, in which a nonlinear switch, or limiter, blends a high-order scheme with a first-order scheme.¹ In more advanced models, the limited approximation is combined with an approximate Riemann solver. Some models use an approximate Riemann solver based on the five waves associated with the fluid dynamics system, and treat the electromagnetic effects using the constrained-transport technique.² The latest models use approximate Riemann solvers based on the waves associated with the full MHD system.³

In this article we outline elements of a modern, solution-adaptive MHD code that we use at the University of Michigan for space-plasma simulations.

MHD Equations

MHD describes the time evolution of conducting fluids. The basic MHD equations combine Maxwell's equations to describe electromagnetic fields and the conservation laws of hydrodynamics. The sources of the electromagnetic fields (electric charge and current densities) are calculated self-consistently with the fluid motion.

Classical MHD

We can write the governing equations for an ideal, nonrelativistic, compressible plasma in many forms. While the MHD equations' different forms describe the same physics at the differential equation level, there are important practical differences when we solve the various formulations' discretized forms.

According to the Lax–Wendroff theorem,⁴ we can expect only conservative schemes to get the correct jump conditions and propagation speed for a discontinuous solution. This fact is emphasized much less in global magnetosphere simulation literature than the more-controversial divergence of \mathbf{B} issue. In some test problems, the nonconservative discretization of the MHD equations can lead to significant errors, which do not diminish with increased grid resolution.

Primitive variable form. In primitive variables, we

can write the governing equations of ideal MHD, which represent a combination of Euler's gasdynamics equations and Maxwell's electromagnetics equations:

$$\frac{\partial \rho}{\partial t} + \mathbf{u} \cdot \nabla \rho + \rho \nabla \cdot \mathbf{u} = 0 \quad (1)$$

$$\rho \frac{\partial \mathbf{u}}{\partial t} + \rho \mathbf{u} \cdot \nabla \mathbf{u} + \nabla p - \frac{1}{\mu_0} \mathbf{j} \times \mathbf{B} = 0 \quad (2)$$

$$\frac{\partial \mathbf{B}}{\partial t} + \nabla \times \mathbf{E} = 0 \quad (3)$$

$$\frac{\partial p}{\partial t} + \mathbf{u} \cdot \nabla p + \gamma p \nabla \cdot \mathbf{u} = 0, \quad (4)$$

where μ_0 and γ represent the magnetic permeability of a vacuum and the specific heat ratio of the gas. In addition, current density \mathbf{j} and electric field vector \mathbf{E} are related to magnetic field \mathbf{B} by Ampère's law and Ohm's law:

$$\mathbf{j} = \frac{1}{\mu_0} \nabla \times \mathbf{B} \quad (5)$$

$$\mathbf{E} = -\mathbf{u} \times \mathbf{B}. \quad (6)$$

Gasdynamics conservation form. For one popular class of schemes, we write the equations in a form in which the gasdynamic terms are in divergence form, and the momentum and energy equations' electromagnetic terms are source terms. This gives

$$\frac{\partial \rho}{\partial t} + \nabla \cdot (\rho \mathbf{u}) = 0 \quad (7)$$

$$\frac{\partial (\rho \mathbf{u})}{\partial t} + \nabla \cdot (\rho \mathbf{u} \mathbf{u} + p \mathbf{I}) = \frac{1}{\mu_0} \mathbf{j} \times \mathbf{B} \quad (8)$$

$$\frac{\partial E_{gd}}{\partial t} + \nabla \cdot [\mathbf{u}(E_{gd} + p)] = \frac{1}{\mu_0} \mathbf{u} \cdot (\mathbf{j} \times \mathbf{B}) \quad (9)$$

for the hydrodynamic flow, and

$$\frac{\partial \mathbf{B}}{\partial t} + \nabla \times \mathbf{E} = 0 \quad (10)$$

for the magnetic field's time evolution. In these equations, \mathbf{I} is the identity matrix and E_{gd} is the gasdynamic total energy, given by

$$E_{gd} = \frac{1}{2} \rho u^2 + \frac{1}{\gamma - 1} p. \quad (11)$$

You can see that the source terms in these equations are entropy preserving.

Fully conservative form. The fully conservative

form of the equations is

$$\frac{\partial \mathbf{U}}{\partial t} + (\nabla \cdot \mathbf{F})^T = 0, \quad (12)$$

where \mathbf{U} is the vector of conserved quantities, and \mathbf{F} is a flux diad,

$$\mathbf{U} = \begin{pmatrix} \rho \\ \rho \mathbf{u} \\ \mathbf{B} \\ E_{mbd} \end{pmatrix} \quad (13)$$

$$\mathbf{F} = \begin{pmatrix} \rho \mathbf{u} \\ \rho \mathbf{u} \mathbf{u} + \left(p + \frac{1}{2\mu_0} B^2 \right) \mathbf{I} - \frac{1}{\mu_0} \mathbf{B} \mathbf{B} \\ \mathbf{u} \mathbf{B} - \mathbf{B} \mathbf{u} \\ \mathbf{u} \left(E_{mbd} + p + \frac{1}{2\mu_0} B^2 \right) - \frac{1}{\mu_0} (\mathbf{u} \cdot \mathbf{B}) \mathbf{B} \end{pmatrix}^T, \quad (14)$$

where E_{mbd} is the magnetohydrodynamic energy, given by

$$E_{mbd} = E_{gd} + \frac{1}{2\mu_0} B^2. \quad (15)$$

Symmetrizable formulation. Sergei Godunov⁵ and many others have studied symmetrizable systems of conservation laws. One property of the symmetrizable form of a system of conservation laws is that we can derive an added conservation law

$$\frac{\partial(\rho s)}{\partial t} + \frac{\partial(\rho s u_x)}{\partial x} + \frac{\partial(\rho s u_y)}{\partial y} + \frac{\partial(\rho s u_z)}{\partial z} = 0$$

for entropy s by linearly combining the system of equations. For the ideal MHD equations, as for the gasdynamic equations, the entropy is $s = \log(p/\rho^\gamma)$. Another property is that the system is Galilean invariant;⁵ all waves in the system propagate at speeds $u \pm c_w$ (for MHD, the possible values of c_w are the Alfvén, magnetofast, and magnetoslow speeds). Neither of these properties holds for the fully conservative form of the MHD equations.

Godunov showed that the fully conservative form of the MHD equations (Equation 12) is not symmetrizable.⁵ We can write the symmetrizable form as

$$\frac{\partial \mathbf{U}}{\partial t} + (\nabla \cdot \mathbf{F})^T = \mathbf{Q}, \quad (16)$$

where

$$\mathbf{Q} = -\nabla \cdot \mathbf{B} \begin{pmatrix} 0 \\ \frac{1}{\mu_0} \mathbf{B} \\ \mathbf{u} \\ \frac{1}{\mu_0} \mathbf{u} \cdot \mathbf{B} \end{pmatrix}. \quad (17)$$

Marcel Vinokur separately showed that we could derive Equation 16 starting from the primitive form, if no stipulation is made about $\nabla \cdot \mathbf{B}$ in the derivation. Kenneth Powell showed that we could use this symmetrizable form to derive a Roe-type approximate Riemann solver for solving the MHD equations in multiple dimensions.³

The MHD eigensystem arising from Equations 12 or 16 leads to eight eigenvalue–eigenvector pairs. The eigenvalues and associated eigenvectors correspond to an entropy wave, two Alfvén waves, two magnetofast waves, two magnetoslow waves, and an eighth eigenvalue–eigenvector pair that depends on which form of the equations we are solving. This last wave (which describes the jump in the normal component of the magnetic field at discontinuities) has a zero eigenvalue in the fully conservative case, and an eigenvalue equal to the normal component of the velocity u_n in the symmetrizable case. The eigenvector expressions and scaling are more intricate than in gasdynamics.

While Equation 12 is fully conservative, the symmetrizable formulation (given by Equation 16) is formally not fully conservative. Terms of order $\nabla \cdot \mathbf{B}$ are added to what would otherwise be a divergence form. The danger of this is that shock-jump conditions might not be correctly met, unless the added terms are small and/or they alternate in sign so that the errors are local and, in a global sense, cancel in some way with neighboring terms. We must weigh this downside, however, against the alternative; a system (the one without the source term) that, while conservative, is not Galilean invariant, has a zero eigenvalue in the Jacobian matrix, and is not symmetrizable.

Semirelativistic MHD

While the solar-wind speed remains nonrelativistic in the solar system, the intrinsic magnetic fields of several planets in the solar system are high enough, and the density of the plasma low enough, that the Alfvén speed

$$V_A = \sqrt{\frac{B^2}{\mu_0 \rho}} \quad (18)$$

can reach appreciable fractions of the speed of light. In the case of Jupiter, the Alfvén speed in the vicinity of the poles is on the order of 10 times the speed of light. Earth has a strong enough intrinsic magnetic field that the Alfvén speed reaches twice the speed of light in Earth’s near-auroral regions.

Limiting the Alfvén speed. For these regions, solving the nonrelativistic ideal MHD equations does not make sense. Having waves in the system propagating faster than the speed of light—besides being nonphysical—causes several numerical difficulties. However, solving the fully relativistic MHD equations is overkill. What is called for is a semi-relativistic form of the equations, in which the flow speed and acoustic speed are nonrelativistic, but the Alfvén speed can be relativistic. A derivation of these semirelativistic equations from the fully relativistic equations is given elsewhere;⁶ we present the final result here. The essence of the derivation is that we must keep the displacement current and, thus, limit the Alfvén speed by the speed of light.

The semirelativistic ideal MHD equations are of the form

$$\frac{\partial \mathbf{U}_{sr}}{\partial t} + (\nabla \cdot \mathbf{F}_{sr})^T = 0, \quad (19)$$

where the state vector \mathbf{U}_{sr} and the flux diad \mathbf{F}_{sr} are

$$\mathbf{U}_{sr} = \begin{pmatrix} \rho \\ \rho \mathbf{u} + \frac{1}{c^2} \mathbf{S}_A \\ \mathbf{B} \\ \frac{1}{2} \rho u^2 + \frac{1}{\gamma - 1} p + e_A \end{pmatrix} \quad (20)$$

$$\mathbf{F}_{sr} = \begin{pmatrix} \rho \mathbf{u} \\ \rho \mathbf{u} \mathbf{u} + p \mathbf{I} + \mathbf{P}_A \\ \mathbf{u} \mathbf{B} - \mathbf{B} \mathbf{u} \\ \left(\frac{1}{2} \rho u^2 + \frac{\gamma}{\gamma - 1} p \right) \mathbf{u} + \mathbf{S}_A \end{pmatrix}. \quad (21)$$

In the preceding equations,

$$\mathbf{S}_A = \frac{1}{\mu_0} (\mathbf{E} \times \mathbf{B}) \quad (22)$$

$$e_A = \frac{1}{2\mu_0} (B^2 + \frac{1}{c^2} E^2) \quad (23)$$

$$\mathbf{P}_A = e_A \mathbf{I} - \frac{1}{\mu_0} \mathbf{B} \mathbf{B} - \frac{1}{\mu_0 c^2} \mathbf{E} \mathbf{E} \quad (24)$$

are the Poynting vector, the electromagnetic energy density, and the electromagnetic pressure tensor, respectively. The electric field \mathbf{E} is related to the magnetic field \mathbf{B} by Ohm's law (Equation 6).

Lowering the speed of light. This new system of equations has wave speeds limited by the speed of light; for strong magnetic fields, the modified Alfvén speed (and the modified magnetofast

speed) asymptote to c . The modified magnetoslow speed asymptotes to a , the acoustic speed. This property offers the possibility of a tricky convergence-acceleration technique for explicit time-stepping schemes, first suggested by Jay Boris;⁷ the wave speeds can be lowered, and the stable time step thereby raised, by artificially lowering the value taken for the speed of light. This method is known as the *Boris correction*.

In the next section, Equations 19 through 24 are valid in physical situations in which $V_A > c$. A slight modification yields a set of equations, the steady-state solutions of which are independent of the value taken for the speed of light. Defining the true value of the speed of light to be c_0 , to distinguish it from the artificially lowered speed of light c , the equations are

$$\frac{\partial \mathbf{U}_{sr}}{\partial t} + (\nabla \cdot \mathbf{F}_{sr})^T = \mathbf{Q}_{c_0}, \quad (25)$$

where the state vector, \mathbf{U}_{sr} , and the flux diad \mathbf{F}_{sr} are as defined in Equations 20 and 21, and the new source term in the momentum equation is

$$\mathbf{Q}_{c_0} = \frac{1}{\mu_0} \left(\frac{1}{c_0^2} - \frac{1}{c^2} \right) \mathbf{E} \mathbf{V} \cdot \mathbf{E}. \quad (26)$$

Numerical Solution Techniques

Numerical solution of the MHD equations starts with discretization of the system of equations to be solved. All discretization schemes introduce errors and other undesirable effects. Modern numerical solution techniques minimize discretization errors and optimize the efficiency of the solution.

Finite-Volume Schemes for Systems of Conservation Laws

We can write a coupled system of conservation laws in the form

$$\frac{\partial \mathbf{U}}{\partial t} + \nabla \cdot \mathbf{F}_{conv} = \mathbf{S}, \quad (27)$$

where \mathbf{U} is the vector of conserved quantities (for example, mass, x -momentum, mass fraction of a particular species, magnetic field, and so on), \mathbf{F}_{conv} is the convective flux, and \mathbf{S} is the source-term modeling diffusion, chemical reactions, and other effects. If necessary, we also can include the transport of radiation in this framework.

Systems of conservation laws lend themselves well to finite-volume discretization. We divide the computational domain into "cells," typically hexahedra or tetrahedra, and integrate the system of partial differential equations given in Equation 27 over each cell in the resulting grid. This leads to a set of coupled ordinary differential equations in

time, with the conserved quantities' cell-averaged values as the unknowns. A conserved physical quantity's rate of change is the sum of all fluxes through the faces defining the cell plus the volume integral of the source terms. This leads to the following ordinary differential equation for the cell volume averaged vector of conserved physical quantities $\bar{\mathbf{U}}$:

$$\frac{d\bar{\mathbf{U}}}{dt} = -\frac{1}{\mathcal{V}} \sum_{\text{faces}} \mathbf{F}_{\text{conv}} \cdot \mathbf{A} + \bar{\mathbf{S}}, \quad (28)$$

where \mathcal{V} is the volume of the cell, \mathbf{A} is the surface area of a given cell face multiplied by the normal vector of the face (the normal vector always points outward of the cell), and $\bar{\mathbf{S}}$ is the volume average of all source terms. Equation 28 provides an inherently 3D update of $\bar{\mathbf{U}}$ and does not separate different directions into different steps (as it is done in operator-splitting methods).

The result is a very physical one: each cell in the grid is a small control volume, in which the integral form of the conservation laws hold. For example, the time rate of change of the average mass in the cell is expressed in terms of flux of mass through the faces of the cell. In this approach, the sophistication level used to compute the fluxes across cell boundaries fundamentally determines the solution's quality.

One distinct advantage of this conservation-law-based finite-volume approach is that we can achieve discontinuous solutions, while obeying proper jump conditions, even at the discrete level. For example, any shocks in a flow will satisfy the Rankine–Hugoniot conditions. While we can achieve this property using a scheme derived from a finite-difference approach, it is a natural consequence of adopting a finite-volume point of view.

High-Resolution Upwind Schemes

Early work in numerical methods for convection-dominated problems showed that results strongly depended on how the spatial derivatives were numerically calculated. The most straightforward methods, obtained by using symmetric centered differences, led to numerically unstable schemes.

Before the development of modern high-resolution upwind schemes, researchers solving hyperbolic systems of conservation laws had a choice between schemes such as Lax–Friedrichs or Rusanov, which were extremely dissipative, or Lax–Wendroff, which was much less dissipative but could not capture even weakly discontinuous solutions (for example, shock waves) without nonphysical and potentially destabilizing oscillations in the solutions.

Over the past half a century, a rich class of schemes became available for numerical solutions of

conservation laws. The basic building blocks were

- Godunov's concept of using the solution to Riemann's initial-value problem as a building block for a first-order numerical method;
- Bram van Leer's insight that Godunov's original scheme could be extended to a higher order by making the scheme nonlinear; and
- work by Philip Roe, van Leer, Stanley Osher, and others on "approximate Riemann solvers," which led to a wide array of schemes that were much less computationally expensive than Godunov's original scheme.

These methods revolutionized computational fluid dynamics and led to the development of modern numerical methods for the solution of MHD equations.

Upwind differencing. The most successful schemes were those that used the convection direction to bias the derivatives' numerical representation. These biased schemes are called upwind schemes, because the data in the update step is biased toward the upwind direction. The simplest upwind scheme for the convection equation

$$\frac{\partial u}{\partial t} + a \frac{\partial u}{\partial x} = 0 \quad (29)$$

is

$$\frac{u_i^{n+1} - u_i^n}{\Delta t} = \begin{cases} -a \frac{u_i^n - u_{i-1}^n}{\Delta x} & a > 0 \\ -a \frac{u_{i+1}^n - u_i^n}{\Delta x} & a < 0 \end{cases}, \quad (30)$$

where i is an index denoting discrete spatial location, and n is an index denoting discrete temporal location.

For systems of conservation laws, use of the upwinding idea relies on

- doing some type of characteristic decomposition to determine which way is upwind for each of the waves of the system and
- constructing an interface flux based on this characteristic decomposition, using upwind-biased data.

The first step makes the scheme stable; the second makes it conservative. There are many ways to carry out the two steps; various approaches lead to a variety of upwind schemes.

Approximate Riemann solvers. The original Godunov scheme⁸ was a finite-volume scheme for so-

lution of inviscid, compressible gas flow equations. This scheme's seminal idea was that at each time step, the fluxes of mass, momentum, and energy through the face connecting two cells of the grid were computed by a solution to Riemann's initial value problem. Specifically, the early interaction between the fluid states in two neighboring cells were computed numerically from the nonlinear, self-similar problem of the wave interactions between the two fluids. This procedure was carried out for a time Δt at each cell-cell interface in the grid, which constituted one iteration.

This scheme, though computationally expensive and only first-order accurate, had a huge impact on computational methods for conservation laws. First, the scheme was extremely robust, even for very strong shocks. It was also much more accurate than the few other schemes that were similarly robust. Finally, researchers soon realized that they could carry the concept to other systems of conservation laws.

Several researchers refined Godunov's scheme by replacing the exact solution of the Riemann problem with approximate solutions that were cheaper, and had certain nice properties.

One of these approximate Riemann solvers that is particularly known because of its high accuracy is Roe's scheme.⁹ We will briefly describe it here for a one-dimensional system of conservation laws; its extension to multiple dimensions is relatively straightforward.

Roe's scheme computes the fluxes at a cell interface based on the states to the left and right of the interface. It looks for simple wave solutions to the system of conservation laws and constructs a numerical flux that treats each of these waves in an upwind manner. If we substitute the relation

$$\mathbf{U}(x, t) = \mathbf{U}(x - \lambda t) \quad (31)$$

into the conservation law

$$\frac{\partial \mathbf{U}}{\partial t} + \frac{\partial \mathbf{F}}{\partial x} = 0, \quad (32)$$

the eigenvalue problem

$$\left(\frac{\partial \mathbf{F}}{\partial \mathbf{U}} - \lambda \mathbf{I} \right) \delta \mathbf{U} = 0 \quad (33)$$

results, where \mathbf{I} is an identity matrix. Roe's scheme is based on the eigenvalues λ_k and right and left eigenvectors R_k and L_k that arise from this eigenvalue problem. In general, for a system of n conservation laws, there will be n eigenvalues, each with a corresponding left and right eigenvector. The Roe flux is expressed in terms of the states \mathbf{U}_L and \mathbf{U}_R just to the left and right of the interface.

We can write it as

- the flux calculated based just on the left state, plus a correction due to waves traveling leftward from the right cell,
- the flux calculated based just on the right state, plus a correction due to waves traveling rightward from the left cell, or
- a symmetric form that arises from averaging the previous two expressions, given by

$$\mathbf{F}_{\text{interface}} = \frac{1}{2} [\mathbf{F}(\mathbf{U}_L) + \mathbf{F}(\mathbf{U}_R)] - \frac{1}{2} \sum_{k=1}^n R_k |\lambda_k| L_k (\mathbf{U}_R - \mathbf{U}_L). \quad (34)$$

Research into approximate Riemann solvers led to robust and low-dissipation schemes. These algorithmic advances yielded methods that had the minimum dissipation necessary to provide stability—they provided robustness nearly equal to that of the Lax–Friedrichs scheme in conjunction with accuracy near that of the Lax–Wendroff scheme. When coupled with the limited-reconstruction techniques, these schemes provided the accurate, robust, efficient approaches that we generally classify as high-resolution methods.

Limited reconstruction. Our approach takes advantage of these advances in approximate Riemann solvers and limited reconstruction. The limited-reconstruction approach ensures second-order accuracy away from discontinuities, while simultaneously providing the stability that ensures nonoscillatory solutions. We use modern limiters to ensure these properties. The approximate Riemann solver approach provides the correct capturing of discontinuous solutions and a robustness across a wide range of flow parameters.

To compute the interface flux, we need interpolated values of the flow states at the interfaces between cells. Since the interface lies halfway between the cell centers on a Cartesian grid, a simple averaging of the two cell center states might seem appropriate. However, we need a more sophisticated interpolation to yield schemes that meet our accuracy and stability criteria.

van Leer proposed a family of limited interpolation schemes, in what is now known as the monotone upstream-centered schemes for conservation laws (MUSCL) approach.¹⁰ To interpolate a variable q to the interface $i + 1/2$ between cell centers i ,

$$q_{i+1/2} = q_i + \frac{1}{4} [(1 + \kappa) \phi(r_{i+1/2}) (u_{i+1} - u_i) + (1 - \kappa) \phi(1/r_{i+1/2}) (u_i - u_{i-1})] \quad (35)$$

In the preceding, κ is a parameter that determines the relative weighting of the upwind and downwind cells in the reconstruction, and ϕ is a limiter function. If ϕ were taken to be zero, the interpolation would be the first-order one—that is, the interface value is the same as the cell-centered value. If ϕ were taken to be one, the reconstruction would be unlimited. For stability's sake, ϕ is a function of the ratio

$$r_{i+1/2} = \frac{u_{i+1} - u_i}{u_i - u_{i-1}}. \quad (36)$$

Popular choices for κ are zero (Fromm's scheme) and minus one (second-order upwind). Popular choices for ϕ include

van Albada

$$\phi(r) = \frac{r + r^2}{1 + r^2}, \quad (37)$$

Minmod

$$\phi(r) = \min\left(1, \frac{(3 - \kappa)}{(1 - \kappa)} r\right), \quad (38)$$

Superbee: $\phi(r) = \max(0, \min(2r, 1), \min(r, 2))$. (39)

$\nabla \cdot \mathbf{B}$ Control Techniques

Another way in which the numerical solution of the MHD equations differs from that of the gasdynamic equations is the constraint that $\nabla \cdot \mathbf{B} = 0$. We can enforce this constraint numerically, particularly in shock-capturing codes, in a number of ways, but each way has its particular strengths and weaknesses. Next, we provide a brief overview of the schemes. (For more complete explanations, refer to the cited references. Gábor Tóth has a numerical comparison of many of the approaches for a suite of test cases.¹¹)

Eight-wave scheme. Kenneth Powell^{3,12} first proposed an approach based on the symmetrizable form of the MHD equations (Equation 16). In this approach, the source term on the right-hand side of Equation 16 is computed at each time step and included in the update scheme. Discretizing this form of the equations leads to enhanced stability and accuracy. However, there is no stencil on which the divergence is identically zero. In most regions of the flow, the divergence source term is small, but it is not guaranteed to be small near discontinuities. In essence, the inclusion of the source term changes what would be a system zero eigenvalue to one whose value is u_n , the component of velocity normal to the

interface through which the flux is computed. We typically refer to the scheme as the eight-wave scheme; the eighth wave corresponds to propagation of jumps in the normal component of the magnetic field.

We can think of the eight-wave scheme as a hyperbolic or advective approach to controlling $\nabla \cdot \mathbf{B}$; symmetrizable form of the equations (Equation 16) are consistent with the passive advection of $\nabla \cdot \mathbf{B}/\rho$. The eight-wave scheme is computationally inexpensive, easy to add to an existing code, and quite robust. However, if there are regions in the flow in which the $\nabla \cdot \mathbf{B}$ source term Equation 17 is large, the numerical errors can create problems such as the generation of spurious magnetic fields.

Projection scheme. Jeremiah Brackbill and Daniel Barnes¹³ proposed using a Hodge-type projection to the magnetic field. This approach leads to a Poisson equation to solve each time the projection occurs:

$$\nabla^2 \phi = \nabla \cdot \mathbf{B} \quad (40)$$

$$\mathbf{B}_{\text{projected}} = \mathbf{B} - \nabla \phi. \quad (41)$$

The resulting projected magnetic field is divergence-free on a particular numerical stencil, to the level of error of the Poisson equation's solution. While it is not immediately obvious that using the projection scheme in conjunction with the fully conservative form of the MHD equations gives the correct weak solutions, Tóth proved this to be the case.¹¹ The projection scheme has several advantages, including the ability to use standard software libraries for the Poisson solution, its relatively straightforward extension to general unstructured grids, and its robustness. It does, however, require solving an elliptic equation at each projection step, which can be expensive, particularly on distributed-memory machines.

Diffusive control. Some of the most recent work on the $\nabla \cdot \mathbf{B} = 0$ constraint relates to modifying the eight-wave approach by adding a source term proportional to the gradient of $\nabla \cdot \mathbf{B}$ so that the divergence satisfies an advection-diffusion equation, rather than a pure advection equation. This technique, referred to as diffusive control of $\nabla \cdot \mathbf{B}$, has the same advantages and disadvantages as the eight-wave approach. It is not strictly conservative, but appears to keep the level of $\nabla \cdot \mathbf{B}$ lower than the eight-wave approach does.

Constrained transport. Several approaches exist

that combine a Riemann-solver-based scheme with a constrained-transport approach. Evans and Hawley's constrained-transport approach treated the MHD equations in the gasdynamics–electromagnetic-split form of Equations 7 through 9.² The grid was staggered, and the $\nabla \cdot \mathbf{B} = 0$ constraint met identically, on a particular numerical stencil.

The advantages of the conservative constrained-transport schemes are that they are strictly conservative and that they meet the $\nabla \cdot \mathbf{B} = 0$ constraint to machine accuracy, on a particular stencil. The primary disadvantage is the difficulty in extending them to general grids. Tóth and Roe¹⁴ made some progress on this front; they developed divergence-preserving prolongation and restriction operators, allowing the use of conservative constrained-transport schemes on h -refined meshes.

However, conservative constrained-transport techniques also lose their $\nabla \cdot \mathbf{B}$ -preserving properties if different cells advance at different physical time rates. This precludes using local time-stepping. Thus, while for unsteady calculations the cost of the conservative constrained-transport approach is comparable to the eight-wave scheme, for steady-state calculations (where we typically would use local time-stepping), the cost can be prohibitive.

Time-Stepping

Because a major goal of global space-plasma simulations is creating a predictive space-weather tool, solution time is a paramount issue; a predictive model must run substantially faster than real time. From the starting point—observing a solar event—to the ending point—postprocessing the data from a simulation based on the initial observational conditions—a simulation must accomplish rapidly to be useful.

The principal limitation of the present generation of global space-plasma codes is the explicit time-stepping algorithm. Explicit time steps are limited by the Courant-Friedrichs-Lewy (CFL) condition, which ensures that no information travels more than one cell size during a time step. This condition represents a nonlinear penalty for highly resolved calculations, because finer grid resolution not only results in more computational cells, but also in smaller time steps.

In global MHD space-plasma simulations, two factors control the CFL condition: the smallest cell size in the simulation and the fast magnetosonic speed in high-magnetic-field, low-plasma-density regions. In a typical magnetosphere simulation, in which the smallest cell size is about $0.25 R_E$, the

CFL condition limits the time step to about 10^{-2} s. The high fast magnetosonic speed (due to the high Alfvén speed) in the near-Earth region primarily controls this small step.

Local Time-Stepping

In the local time-stepping approach, a local stability condition determines the time step for each cell in a computational domain. The flow variables in cell i are advanced from time step n to time step $n + 1$ as

$$U_i^{n+1} = U_i^n + \Delta t_i^n (-\nabla \cdot \mathbf{F} + Q)_i, \quad (42)$$

where the stability condition determines the local time step. Here, U represents the conservative state vector, \mathbf{F} is the flux diad, and Q is the source term. In case of ideal MHD, the time step is determined by the CFL condition

$$\Delta t_i^n = C \frac{\Delta x_i}{c_i^{fast} + |u_i|}, \quad (43)$$

where $C < 1$ is the Courant number and c_i^{fast} is the fast speed in cell i . In more than one dimension, we use the sum of the speeds in all directions in the denominator.

This technique is different from subcycling, in which cells advance at the same physical time rate, but the number of time steps individual cells take varies. For example, in adaptive grids, usually we set the time step to be inversely proportional to cell size, so that a finer cell typically makes two half time steps while the coarser cell makes only one full time step. In this method, a global stability condition determines the time steps compared with local time-stepping in which time steps are set on a cell-by-cell basis.

Equation 42 shows that if a steady-state solution exists, it satisfies

$$0 = (-\nabla \cdot \mathbf{F} + Q)_i \quad (44)$$

because in steady state, $U_i^{n+1} = U_i^n$, and we can simplify with the time step Δt_i^n , which always is a positive number. Consequently, the steady-state solution is independent of the time step, so it does not matter if it is local or global.

The preceding proof assumes that the boundary conditions fully determine the steady state. This is a nontrivial assumption because the MHD equations are nonlinear. Initial boundary value problems might or might not asymptote to steady states independent of the initial conditions; it depends on the boundary conditions imposed, which are problem dependent. In practice, magnetosphere simulations seem to converge to the same solution independent of the initial conditions or the

time-integration scheme.

The applicability of the local time-stepping technique in a given scheme depends primarily on the evolution of $\nabla \cdot \mathbf{B}$. In some methods, even if $\nabla \cdot \mathbf{B} = 0$ initially, the numerical transients toward steady state will destroy this property with the application of local time-stepping. For instance, we can show that the constrained transport scheme can't be combined with local time-stepping. In our code, we use constrained transport only in time-accurate simulations, local time-stepping with the eight-wave method.

Implicit Time-Stepping

The simplest and least-expensive time-stepping scheme is multistage explicit time-stepping, in which the CFL stability condition limits a time step. We also have an unconditionally stable fully implicit time-stepping scheme. This second-order implicit time discretization requires solving a system of nonlinear equations for all flow variables at each time step. We can achieve this by using the Newton–Krylov–Schwarz approach: applying a Newton iteration to the nonlinear equations, solving them using a parallel Krylov type iterative scheme, and accelerating the Krylov solver convergence with a Schwarz-type preconditioning. Because every block has a simple Cartesian geometry, we can implement the preconditioner very efficiently. The resulting implicit scheme requires about 20 to 30 times more CPU time per time step than the explicit method, but the physical time step can be 1,000 to 10,000 times larger. This implicit algorithm has very good parallel scaling because of the Krylov scheme and the block-by-block preconditioner application. While our scaling for the implicit is quite good, it's not as near perfect as the explicit, because of the higher amount of inter-processor communication overhead.

We also can combine explicit and implicit time-stepping. Magnetosphere simulations include large volumes in which the Alfvén speed is quite low (tens of km/s), and the local CFL number allows large, explicit time steps (tens of seconds to several minutes). In these regions, implicit time-stepping is a waste of computational resources. Because the parallel implicit technique we use is fundamentally block based, we implicitly treat only those blocks where the CFL condition would limit the explicit time step to less than the selected time step (typically, approximately 10 s). This combined explicit–implicit time-stepping represents more computational challenges (such as separate load balancing of explicit and implicit blocks). Overall, this solution seems to be a very promising option, but we need to explore other potential avenues before we make a final decision about

the most efficient time-stepping algorithm for space MHD simulations.

Data Structure and Adaptive Mesh Refinement

Adaptive mesh refinement (AMR) techniques that automatically adapt the computational grid to the solution of the governing PDEs are very effective in treating problems with disparate length scales. They avoid underresolving the solution in interested regions (for example, high gradient) and, conversely, avoid over-resolving the solution in other less-interesting regions (low gradient), thereby saving orders of magnitude in computing resources for many problems. For typical solar-wind flows, length scales can range from tens of kilometers in the near Earth region to the Earth–Sun distance (1.5×10^{11} m), and timescales can range from a few seconds near the Sun to the expansion time of the solar wind from the Sun to Earth ($\sim 10^5$ s). The use of AMR is extremely beneficial and almost a virtual necessity for solving problems with such disparate spatial and temporal scales.

Block-Adaptive AMR

We developed a simple and effective block-based AMR technique used with the finite-volume scheme previously described. We integrate the governing equations to obtain volume-averaged solution quantities within rectangular Cartesian computational cells. The computational cells are embedded in regular structured blocks of equal-sized cells. The blocks are geometrically self-similar. Typically, the blocks we use consist of anywhere between $4 \times 4 \times 4 = 64$ and $12 \times 12 \times 12 = 1,728$ cells (see Figure 1). We store solution data associated with each block in standard indexed array data structures, making it straightforward to obtain solution information from neighboring cells within a block.

Computational grids are composed of many self-similar blocks. Although each block within a grid has the same data-storage requirements, blocks can be of different sizes in terms of the volume of physical space they occupy. Starting with an initial mesh consisting of blocks of equal size (that is, equal resolution), we accomplish adaptation by dividing and coarsening appropriate solution blocks. In regions requiring increased cell resolution, a parent block is refined by dividing itself into eight children, or offspring. Each of the eight octants of a parent block becomes a new block with the same number of cells as the parent, which doubles cell resolution in the region of interest. Conversely, in over-resolved regions, the refinement process reverses; eight children coarsen and coalesce into a single parent block. Thus, cell resolution reduces by a fac-

tor of 2. We use standard multigrid-type restriction and prolongation operators to evaluate the solution on all blocks created by the coarsening and division processes, respectively.

Figure 1 shows two neighboring blocks, one refined and one that isn't. Any block can be refined, successively leading to finer blocks. In the present method, we constrain mesh refinement such that the cell resolution changes by only a factor of 2 between adjacent blocks; the minimum resolution is not less than the initial mesh's.

To independently apply the update scheme for a given iteration or time step directly to all blocks, adjacent blocks—those with common interfaces—share some additional solution information. This information resides in an additional two layers of overlapping ghost cells associated with each block. At interfaces between blocks of equal resolution, these ghost cells simply take on the solution values associated with the appropriate interior cells of the adjacent blocks. At resolution changes, restriction and prolongation operators, similar to those used in block coarsening and division, evaluate the ghost-cell solution values. After each stage of the multistage time-stepping algorithm, ghost-cell values reevaluate to reflect the updated solution values of neighboring blocks. The AMR approach also requires additional interblock communication at interfaces with resolution changes to strictly enforce the flux conservation properties of the finite-volume scheme. In particular, we use the interface fluxes computed on more refined blocks to correct the interface fluxes computed on coarser neighboring blocks to ensure that the fluxes are conserved across block interfaces.

Hierarchical Tree Data Structure

We use a hierarchical tree-like data structure with multiple roots and trees and additional interconnects between the tree leaves to track mesh refinement and the connectivity between solution blocks. Figure 2 depicts this interconnected data structure "forest." The blocks of the initial mesh are the forest roots, which reside in an indexed array data structure. Associated with each root is a separate octree data structure that contains all the blocks making up the tree leaves created from the original parent blocks during mesh refinement. Each grid block corresponds to a tree node. To determine block connectivity, we can traverse the multitree structure by recursively visiting the parent and children solution blocks. However, to reduce overhead associated with accessing solution information from adjacent blocks, we compute and store the neighbors of each block directly, providing interconnects between blocks in the hierarchical data structure that

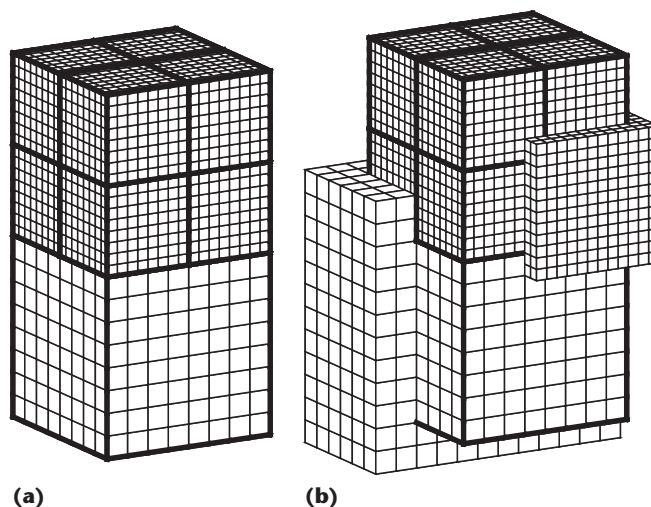


Figure 1. Self-similar blocks. (a) Those used in parallel block-based adaptive mesh refinement schemes, and (b) illustrating the double layer of ghost cells for both coarse and fine blocks.

are neighbors in physical space.

An advantage of the preceding hierarchical data structure is that it is relatively easy to carry out local mesh refinement anytime during a calculation. For example, if a particular flow region becomes sufficiently interesting at some point in a computation, we can obtain better resolution of that region by refining its solution blocks, without affecting the grid structure in other regions of the flow. Reducing grid resolution in a region is equally easy. There is no need to completely remesh the entire grid and recalculate block connectivity with each mesh refinement. Although other approaches are possible, ours directs block coarsening and dividing via multiple physics-based refinement criteria. In particular, we base decisions about when to refine or coarsen blocks on comparisons of the maximum values of various local flow quantities determined in each block to specified refinement threshold values. Note that we dynamically adjust the refinement thresholds to control a calculation's total number of blocks and cells. We can use other refinement criteria, such as a combination of estimated numerical errors.

Figure 3 illustrates the adaptation of the block-based Cartesian mesh to an evolving solution. It shows the grid at four time instances for an unsteady calculation, showing the solution blocks (thick lines) and computational cells (thin lines) of the evolving grid. As previously noted, each grid refinement level introduces cells smaller in dimension by a factor of 2 from those one level higher in the grid. Typically, calculations might have 10 to 15 refinement levels; some

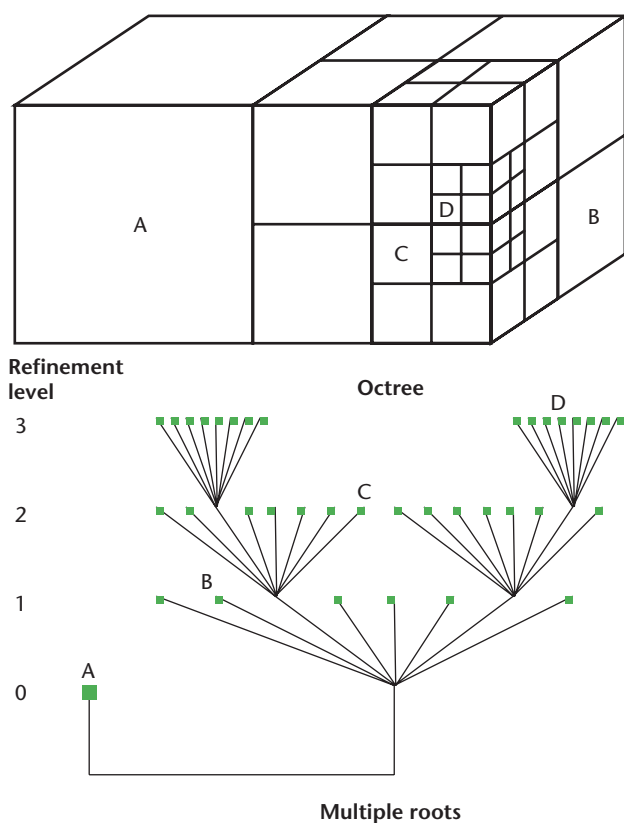


Figure 2. Solution blocks of a computational mesh with three refinement levels originating from two initial blocks and the associated hierarchical multiroot octree data structure. The figure omits interconnects to neighbors.

calculations could have more than 20. With 20, the finest cells on the mesh are more than one million times (2^{20}) smaller in each dimension than the coarsest cells. The block-based AMR approach previously described has many similarities to the cell-based method proposed by De Zeeuw and Powell.¹² Although the block-based approach is somewhat less flexible and incurs some solution resolution inefficiencies compared with a cell-based approach, it offers many advantages when we consider parallel algorithm implementations and performance issues. Next, we look at how block adaptation readily enables domain decomposition and effective load balancing and leads to low communication overhead between solution cells within the same block.

Parallel Implementation

We designed the parallel block-based AMR solver from the ground up, aiming to achieve very high performance on massively parallel architectures. The underlying upwind finite-volume solution algorithm, with explicit time-stepping, has a very

compact stencil, making it highly local. The hierarchical data structure and self-similar blocks readily simplify domain decomposition and readily enable good load-balancing, a crucial element for truly scalable computing. Natural load-balancing occurs by distributing the blocks equally among the processors. We achieve additional optimization by ordering the blocks using the Peano–Hilbert space-filling curve to minimize interprocessor communication. The self-similar nature of the solution blocks also means that serial performance enhancements apply to all blocks and that fine-grained algorithm parallelization is possible. The algorithm’s parallel implementation is so pervasive that even the grid adaptation performs in parallel.

Other features of the parallel implementation include using Fortran 90 as the programming language and the message-passing interface (MPI) library for performing the interprocessor communication. Use of these standards greatly enhances code portability and leads to very good serial and parallel performance. Message passing occurs asynchronously, with gathered wait states and message consolidation.

We implemented these new methods in the block adaptive-tree solar-wind Roe-type upwind scheme (BATS-R-US) code developed at the University of Michigan.^{6,12} BATS-R-US solves the relativistic MHD equations using block-based AMR technology, finite-volume methodology with four approximate Riemann solvers (Roe,⁹ Linde,¹⁶ artificial wind,¹⁷ and Lax-Friedrichs/Rusanov), four different divergence **B** control techniques (eight-wave, constrained transport, projection, and $\nabla \cdot \mathbf{B}$ diffusion), and your choice of five limiters. You also can choose different time-stepping methods (local, explicit, implicit, and combined explicit and implicit) depending on the type of problem you want to solve.

We’ve implemented the algorithm on Cray T3E supercomputers, SGI and Sun workstations, Beowulf-type PC clusters, SGI shared-memory machines, a Cray T3D, several IBM SP2s, and Compaq supercomputers. BATS-R-US nearly perfectly scales to 1,500 processors and a sustained speed of 342 GFlops has been attained on a Cray T3E-1200 using 1,490 processors. For each target architecture, we use simple single-processor measurements to set the adaptive block size. Figure 4 shows the scaling of BATS-R-US on various architectures.

Applications to Space Weather Simulations

Researchers have applied BATS-R-US to global numerical simulations of the inner heliosphere including coronal mass ejection (CME) propagation,¹⁸ the coupled terrestrial

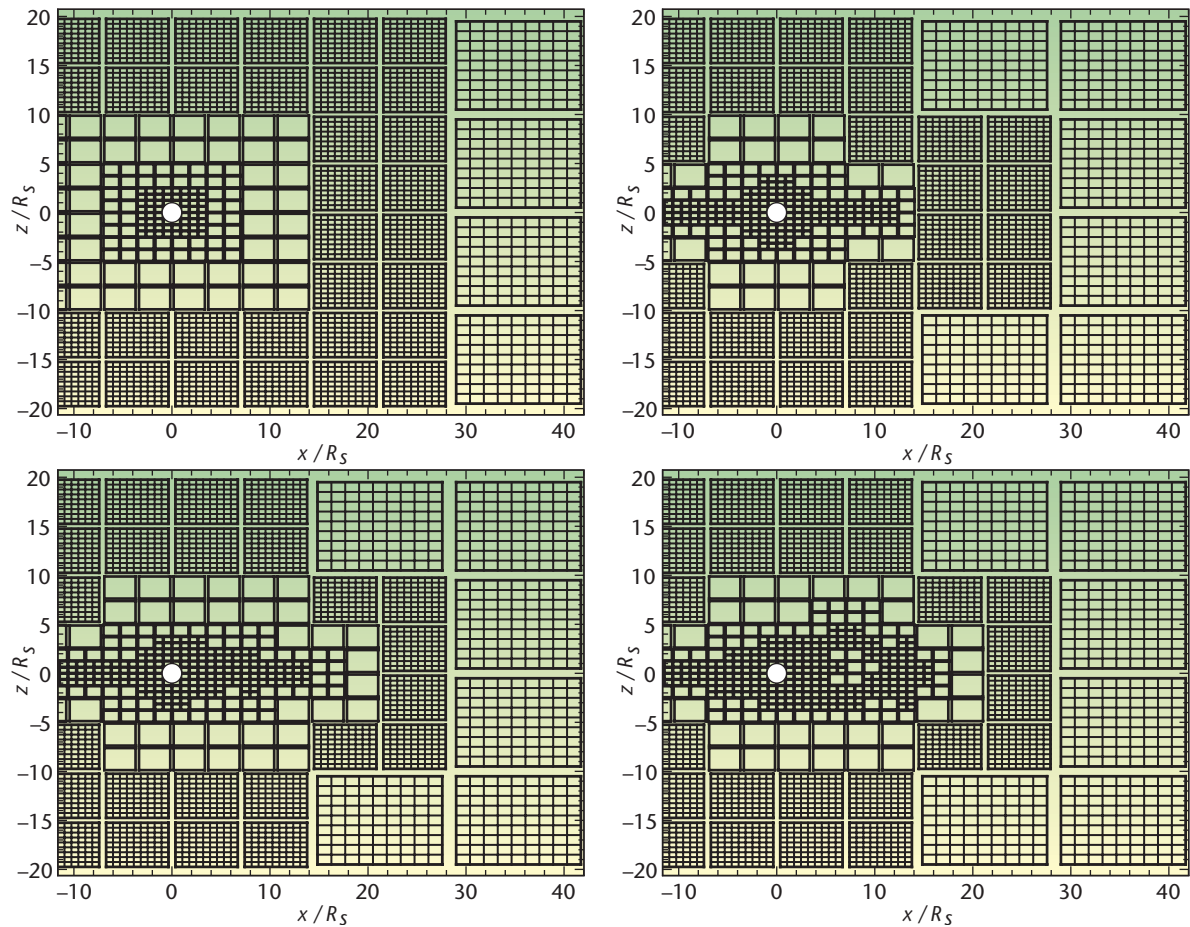


Figure 3. Evolution of a computational mesh illustrating grid adaptation in response to numerical solution changes. The cross-sectional cuts through a 3D grid are for a solar-wind calculation at four different time instances. The computational cells are not shown for the smaller blocks.

magnetosphere–ionosphere,^{19, 20} and the interaction of the heliosphere with the interstellar medium.²¹ Other applications include a host of planetary problems ranging from comets,^{22, 23} to the planets Mercury,²⁴ Venus,²⁵ Mars,²⁶ and Saturn,²⁷ to planetary satellites.^{28, 29} Next, we present a selection of space-weather-related simulations that are most relevant for practical applications.

Space Weather

“Space weather” refers to conditions on the Sun and in the solar wind, magnetosphere, ionosphere, and thermosphere that can influence the performance and reliability of space-borne and ground-based technological systems; it can affect human life or health as well. Adverse conditions in the space environment can disrupt satellite operations, communications, navigation, and electric power distribution grids, leading to broad socioeconomic losses.

The solar corona is so hot ($> 10^6$ K) that in open magnetic field regions, it expands transonically, filling all of interplanetary space with a supersonic magnetized plasma flowing radially outward from the Sun. As this flowing plasma—the solar wind—passes the Earth, it interacts strongly with the geomagnetic field, severely compressing the field on the Earth’s dayside, and drawing it out into a long, comet-like tail on the nightside. The confined region of geomagnetic field is called the Earth’s magnetosphere.

The solar wind not only confines the terrestrial magnetic field within the magnetospheric cavity, but it also transfers significant mass, momentum, and energy to the magnetosphere, as well as to the ionosphere and upper atmosphere. One dramatic consequence of this solar wind and magnetosphere interaction is the production of a variety of complex electric current systems, ranging from a sheet of current flowing on the solar wind and magnetosphere boundary, to an enormous current ring

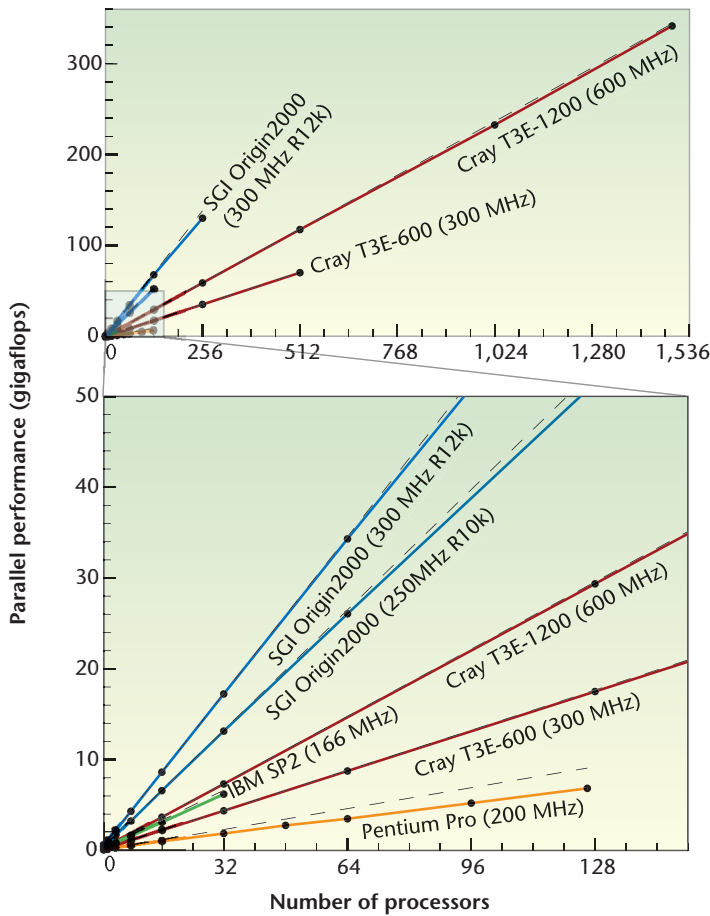


Figure 4. Parallel speedup of BATS-R-US on various architectures. Black dashed lines represent perfect scaling from single-node performance.

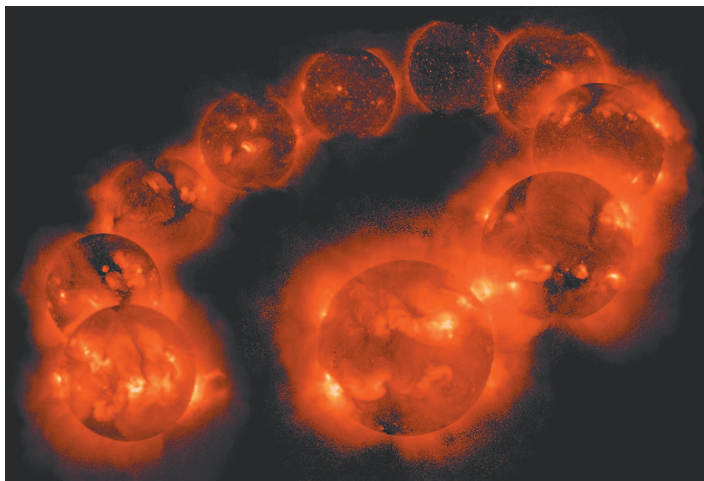


Figure 5. Twelve X-ray images of the Sun obtained by the Yohkoh satellite at 90-day increments provide a dramatic view of how the solar corona changes from solar maximum to minimum. As we approach solar maximum, the reverse progression will occur. (Image courtesy of Lockheed Martin.)

flowing around Earth in the inner magnetosphere, to currents flowing throughout the ionosphere and connecting along magnetic field lines to magnetospheric currents systems. Solar wind–magnetosphere interaction also produces populations of very energetic particles stored in the magnetosphere and precipitated into the upper atmosphere. The electric currents and the energetic particles can have severe consequences for many human activities from ground to space. The variation over time of these electric current systems and energetic particle populations in the geospace environment modulates the consequences for human activities.

Space-weather timescales range from minutes to decades. The longest timescales usually considered important to space weather are the 11-year solar activity cycle and the 22-year solar magnetic cycle (see Figure 5). Near the solar-activity cycle minimum, the solar wind is nearly completely dominated by a quasi-steady outflow.

Significant temporal solar-wind speed variations at Earth’s orbit routinely occur in response to the rotation with the Sun of quasi-steady solar-wind structures. The wind’s large-amplitude Alfvén waves produce large fluctuations in the southward component of the interplanetary magnetic field (IMF). CMEs—the transient mass and magnetic field ejection from the solar corona—also produce solar-wind speed and magnetic field variations. Indeed, the most severe storms experienced in the Earth’s space environment are driven by exceptionally fast CMEs that exhibit a strong southward magnetic field component throughout a significant fraction of their volume. These very fast CMEs, which are ejected from the corona at speeds of more than 1,000 km/s, also drive strong hydromagnetic shocks. These shocks are efficient producers of energetic particles, which can impact the geospace environment. Of course, a very fast CME only is effective at producing a severe geomagnetic storm when it travels toward Earth, which presents a problem for those attempting to give forewarning of such storms.

Figure 6 illustrates this interaction. Figure 6a depicts the CME-generated magnetic cloud approaches the quiet magnetosphere. In Figure 6b, the cloud initiates a stronger interaction that generates stronger magnetospheric current systems and larger, more energetic, magnetospheric particle populations—a geomagnetic storm. As solar activity increases, the frequency of CMEs increases substantially, and the “severity of space weather” concomitantly increases.

Magnetosphere Simulations

The magnetosphere’s steady-state topology for due south- and north-pointing IMF conditions is of great theoretical interest for magnetospheric physics. In an

idealized situation (assuming a nonrotating planet with a strictly southward pointing magnetic dipole moment), such configurations exhibit two planes of symmetry (the equatorial plane and the noon–midnight meridian). Scientists have researched the due south and north IMF configurations countless times.

Our group used BATS-R-US simulations to investigate the solar wind–terrestrial magnetosphere interaction under northward IMF conditions.²⁰ Figure 7 shows a 3D representation of the simulated magnetospheric topology for northward IMF conditions. White solid lines represent the last closed magnetic field lines in the Northern hemisphere, in effect tracing the magnetopause (the discontinuity separating the shocked solar wind from the region dominated by the terrestrial magnetic field). The color code in the equatorial plane represents the thermal pressure distribution of magnetospheric particles.

Figure 8a shows simulation results for the noon–midnight meridian for the Northern hemisphere. The upstream conditions are $n = 5 \text{ cm}^{-3}$, $u = 400 \text{ km/s}$, acoustic Mach number = 8, specific heat ratio = 5/3, and IMF magnitude = 5 nT. The white lines with arrowheads are magnetic field lines. The color coding represents the logarithm of the thermal pressure. The thick red lines indicate topological boundaries that separate flows of distinct characteristics. Figure 8b shows the equatorial plane for the morning side. White lines with arrowheads are streamlines, and color coding represents the sonic Mach number.

Figure 8 shows that a bow shock forms in front of the magnetosphere. This fast magnetosonic shock decelerates, deflects, and heats the solar-wind plasma. The magnetosphere is essentially closed except for a small region near the cusp where the IMF and magnetospheric field reconnect.

In the noon–midnight meridian plane, both the magnetic field and the velocity have no component normal to the plane. In ideal MHD, the magnetic field lines and streamlines are equipotentials because the electric field is perpendicular to both magnetic field and velocity. The magnetic field lines in the noon–midnight meridian plane can be of the same potential if they are on the same streamline. The red thick lines in Figure 8a separate different flow regions and, hence, regions with different potentials.

For symmetry reasons the magnetic field has no component in the equatorial plane; the magnetic field is always perpendicular to the $Z = 0$ plane and points northward everywhere in our case. In contrast, plasma streamlines do not leave the equatorial plane, meaning that the motional electric field is in the equatorial plane and normal to the streamlines. The potential difference between two given streamlines in the equatorial plane remains the same

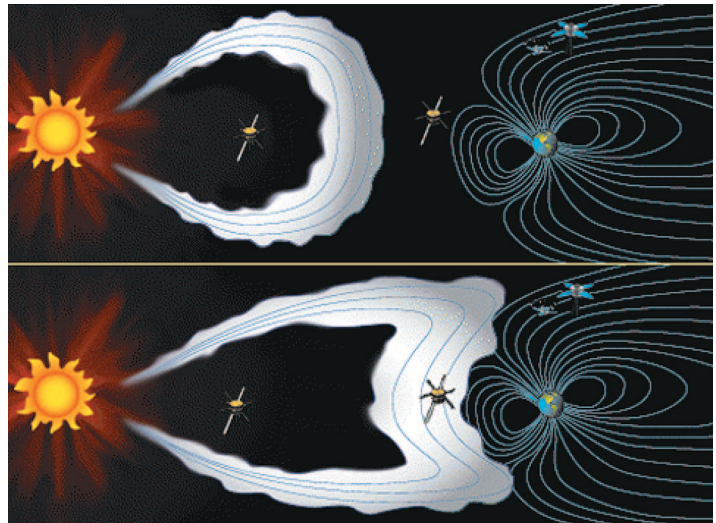


Figure 6. The interaction of the magnetosphere with an expanding magnetic cloud. The coronal mass ejection releases a huge amount of magnetized plasma that propagates to Earth orbit in a few days. When such a cloud hits Earth, intense geomagnetic storms are generated. (Illustration courtesy of the NASA International Solar Terrestrial Program.)

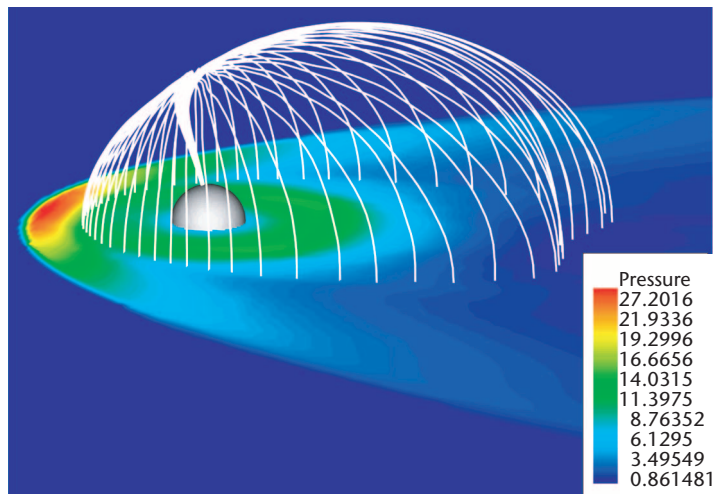


Figure 7. 3D representation of the simulated magnetospheric topology for northward interplanetary magnetic field conditions. White solid lines represent the last closed magnetic field lines in the Northern hemisphere. The color code in the equatorial plane represents the magnetospheric particles' thermal pressure distribution.

throughout the plane. Magnetospheric electric currents are associated with the distortion of the magnetic field from the dipole magnetic field. Stretching the magnetic field generates currents in a clockwise direction while compressing it produces a counterclockwise current in the equatorial plane. The Lorentz force associated with these currents always tends to restore the dipole magnetic field

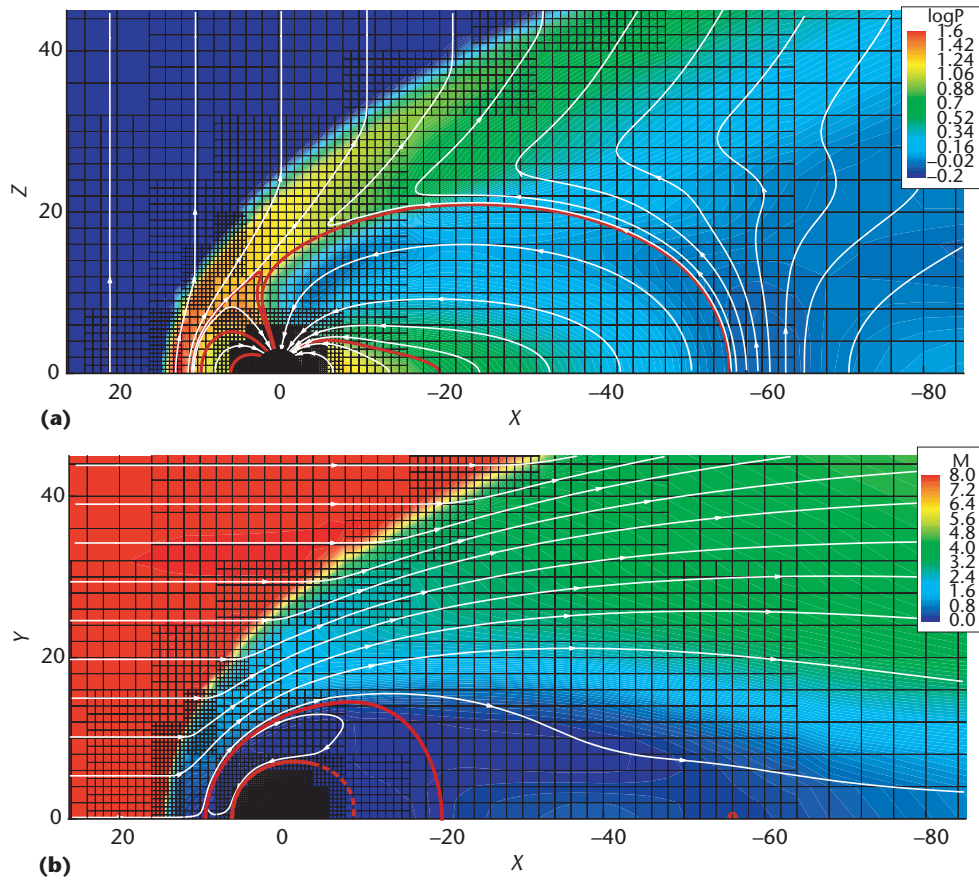


Figure 8. Simulation results for northward interplanetary magnetic field. (a) Noon–midnight meridian for the Northern hemisphere. The white lines are magnetic field lines. The color coding represents the logarithm of the thermal pressure. The thick red lines indicate the topological boundaries that separate flows of distinct characteristics. (b) Equatorial plane for the morning side. White lines are streamlines and the color coding represents the Mach number. The two red lines indicate the boundaries between distinct flow regions.

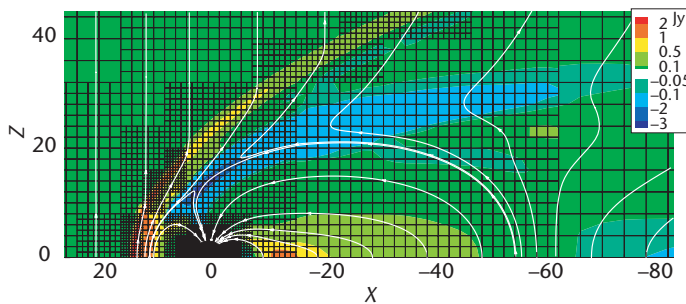


Figure 9. Currents in the noon–midnight meridian plane. The color coding shows the Y component of the current density.

geometry in the closed magnetic field line region. These currents' divergence or convergence within the closed magnetic field line region generates the field-aligned currents flowing out of the equatorial

plane. These field-aligned currents map into the ionosphere. However, the equatorial region's major current component of the distant tail does not converge–diverge within the magnetosphere. It is closed via the magnetopause current in the tail region.

Figure 8 also reveals three topologically distinct regions in the magnetosphere: the inner core or plasmasphere, the outer magnetosphere, and the low-latitude boundary layer (LLBL)–tail region. These regions are separated by boundaries marked by thick red lines.

Figure 9 shows the Y component of the electric currents in the noon–midnight meridian plane. On the day side, most of the currents are generated at the bow shock. These currents' Lorentz force decelerates the solar-wind flow. Most of the magnetopause current appears in the region upstream of the first closed magnetospheric field line. Observations of the sheath transition layer, or plasma-

depletion layer, are consistent with this region of current. The topological boundary itself contains little current and marks the inner edge of the magnetopause current. Observations show that for northward IMF, the topological change occurs at the inner edge of the sheath transition layer.

On the night side, the magnetopause current and the magnetosphere's topological boundary become completely different. In the noon–midnight meridian plane, most of the current is associated with magnetic field kinks located around 20 to 30 R_E above and below the equator; a region few satellites have visited. If we use this current to define the boundary of the magnetosphere, the magnetosphere would appear to be open. Between the last closed field lines and the magnetopause current, magnetic field and particle characteristics are similar to (and observationally difficult to distinguish from) those in the closed magnetic field line region in the magnetotail. This is quite natural because these field lines have just recently lost their topological connection with Earth. It will take an Alfvén traveling time for the field lines to communicate to the flux tube's equatorial region about the magnetic field line being disconnected at the cusp. It will take even longer before the plasma on these flux tubes assimilates to the solar wind.

Solar Simulations

Traditionally, we've defined CMEs as large-scale expulsions of plasma from the corona seen as bright arcs in coronagraphs that record Thomson scattered light. These events are the most stunning activity of the solar corona in which typically 10^{15} to 10^{16} g of plasma is hurled into interplanetary space with a kinetic energy of the order 10^{31} to 10^{32} ergs. Observations show that most CMEs originate from the disruption of large-scale coronal structures known as helmet streamers, arcade-like structures commonly found in coronagraph images.

Central to understanding CME dynamics is the pre-event magnetic field's nature. For a helmet streamer to be in static equilibrium, the underlying magnetic field must be in a closed configuration to confine the dense plasma that would otherwise be carried out with the solar wind. Observations show that the photospheric magnetic field associated with helmet streamers is in a bipolar configuration, with a neutral line separating opposite magnetic polarities. The magnetic field configuration of pre-event helmet streamers is a sheared arcade, possibly containing a flux rope coinciding with the plasma cavity. CMEs could represent a significant restructuring of the global coronal magnetic field.

We carried out a set of numerical simulations³⁰ to test an analytical model for the initiation of

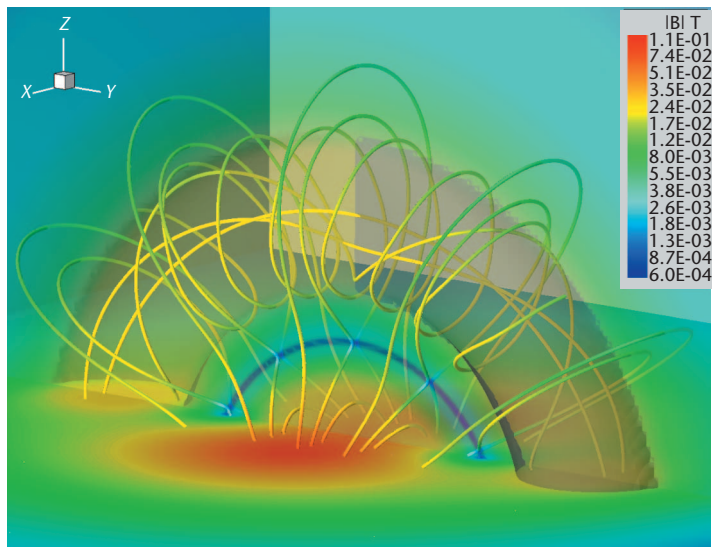


Figure 10. 3D view of the magnetic field configuration for the initial state. Solid lines are magnetic field lines, where the color code visualizes the magnetic field strength in [T]. The surface shaded in gray is an iso-surface of $B_z = 0$.

CMEs developed by Vyacheslav Titov and Pascal Démoulin.³¹ They derived their model from a long line of previous analytical models containing flux ropes suspended in the corona by a balance between magnetic compression and tension forces. Figure 10 shows the initial state of the simulation.

The flux rope undergoes an increasing acceleration, with its upward motion eventually forming a current sheet at the pre-existing X-line's location. Once the current sheet starts forming, the flux rope begins to decelerate. The effects of the line-tying at the ends of the flux rope also might contribute to this deceleration. Another effect that we see at this time (which is an entirely 3D effect) is that torsional Alfvén waves transport most of the magnetic helicity from the flux-rope's footprints toward its top. As a result, the restraining effect caused by the flux-rope feet's line-tying becomes important.

Figure 11 shows a 3D view of the magnetic field configuration at $t = 35$ min. A close look at the flux-rope footprints reveals closed loops connecting the two flux regions. The most plausible explanation of this structure is that there is an interchange reconnection between the highly twisted flux-rope field lines and the overlying closed field lines from the dipole region. As a result of this process, the newly created closed field lines connect the two flux regions, while the highly twisted field lines originate from the dipole field region. The iso-surface of $B_z = 0$ (shaded in gray) in Figure 10 indicates where this process preferentially takes place.

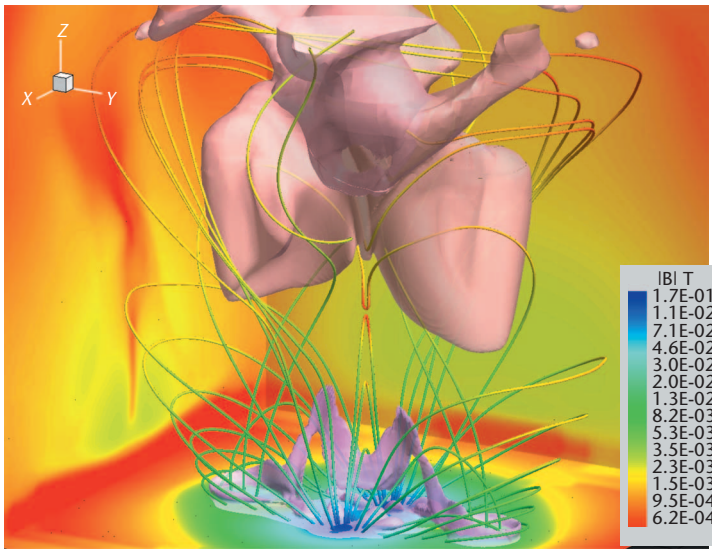


Figure 11. 3D view of the magnetic field configuration at $t = 35$ min. As in Figure 10, the solid lines are magnetic field lines. The color (reversed to that in Figure 10) shows the magnetic field strength. The lower surface shaded in purple is an iso-surface of electric current density of magnitude 0.0015 A/m^2 . The upper surface shaded in maroon is an iso-surface of flow velocity of magnitude 200 km/s .

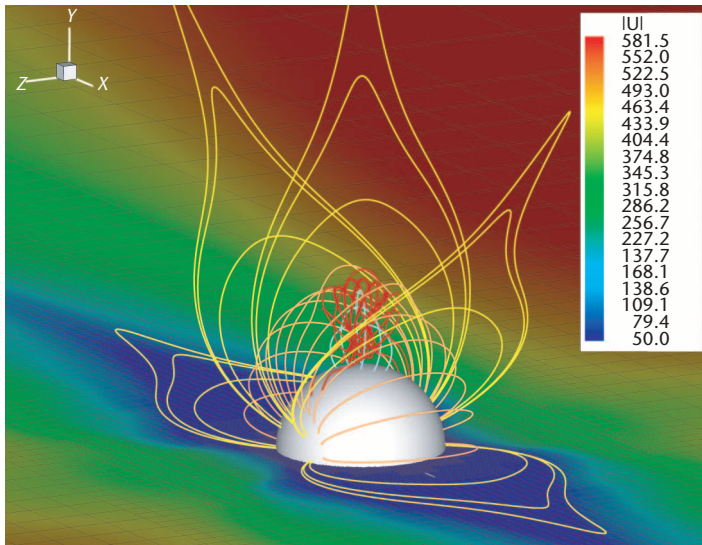


Figure 12. 3D representation of the coronal magnetic field drawn as solid colored lines at $t = 0$ hours. Red and blue lines represent the flux rope. Orange and yellow lines show the poloidal field of the steady-state equatorial streamer belt. On the x - z plane, the computational mesh is represented by thin black lines superimposed on a false-color image of the velocity magnitude.

Simulations of Solar Eruptions

Only in the last few years have CME models been produced that allow for 3D spatial structures. The

approach we take to modeling CMEs is to start with a system that is initially out of equilibrium and simulate its subsequent time evolution. We begin by numerically forming a steady-state corona model along with a bimodal solar wind (slow solar wind near the equator and fast wind at high solar latitudes). The model coronal magnetic field is representative of a solar minimum configuration with open polar field lines and low latitude closed field lines forming a streamer belt. Having attained this steady state, we superimpose a 3D magnetic flux rope and its entrained plasma into the streamer belt of our steady-state coronal model (see Figure 12).³² The flux rope we employ comes from the Sarah Gibson and Boon Chye Low³³ family of analytic solutions of the ideal MHD equations describing an idealized, self-similar expansion of a magnetized cloud resembling a CME. This configuration allows the system to contain substantial free energy. In the subsequent time evolution of the system, we find that the flux rope expands rapidly, driving a strong shock ahead of it as it is expelled from the corona along with large amounts of plasma mimicking a CME. Including this flux rope in a numerical, steady-state corona and solar-wind model extends the Gibson–Low model to address its interaction with the background solar wind.

Figure 13 displays the CME's time evolution, with a time series of figures showing the system at $t = 1.0, 2.0, 3.0,$ and 4.0 hours. The figure depicts the system in 2D equatorial slices. The panels show false-color images of the plasma velocity magnitude on which solid white lines are superimposed representing the magnetic field.

We find the flux rope rapidly expanding and being expelled from the corona while decelerating. An MHD shock front moves ahead of the flux rope, traveling at nearly the same speed as the rope on the y axis while propagating far ahead to the sides of the rope. In effect, the shock front moves at relatively uniform speed, initially forming a spherical bubble, while the flux rope inside the front moves forward faster than it expands to the sides. The ambient solar wind's structure has a profound influence on the shock front. The wind and magnetosonic speeds are minimal in the heliospheric current sheet and both grow with heliospheric latitude. As a result, the shock travels at higher latitude in the fast solar wind with a lower Mach number than found at low latitude.

Our 3D numerical MHD model of a high-speed CME possesses many of the observed bulk characteristics such as total mass and energy and also is representative of basic features such as shock formation and related deceleration. Our model's success in capturing many properties of CMEs, including pre-event structures and background solar

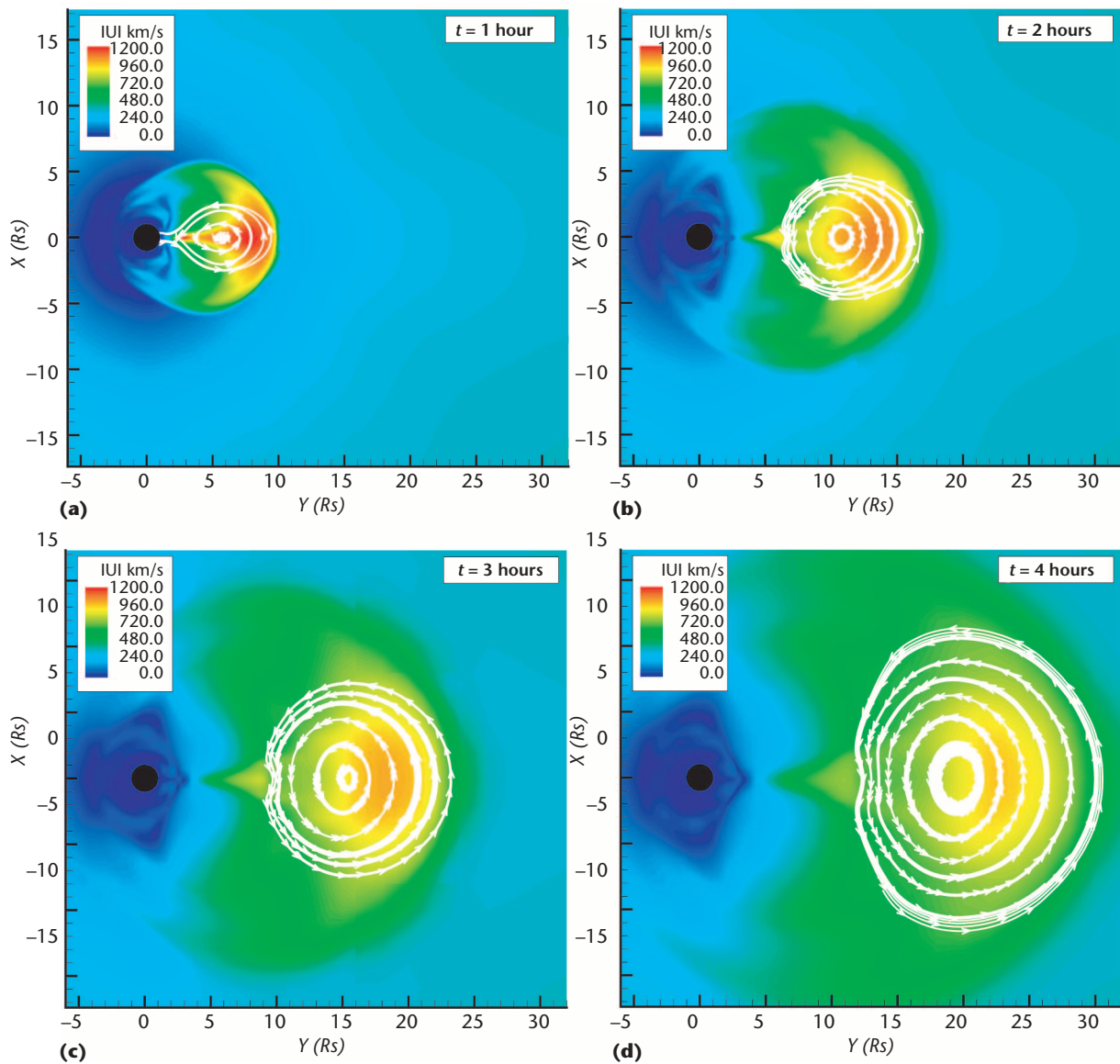


Figure 13. Time sequence of the coronal mass ejection in the equatorial plane at (a) $t = 1$ hour, (b) $t = 2$ hours, (c) $t = 3$ hours, and (d) $t = 4$ hours. Solid white lines display magnetic streamlines (two-dimensional projections of 3D magnetic field lines) superimposed on a color image of the velocity magnitude.

wind, suggests its value for studying CME propagation and space-weather phenomena.

Sun-to-Earth Simulation

In our most ambitious project to date, we used BATS-R-US to simulate an entire space-weather event, from its generation at the Sun through the formation and evolution of a CME, to its interaction with the magnetosphere–ionosphere system. An earlier simulation successfully demonstrated the feasibility of such end-to-end simulations, but it suffered from relatively low resolution. In the original simulations, we used a couple of million cells to describe the entire Sun–solar

wind–magnetosphere–ionosphere system with a density pulse near the Sun generating the CME.

In the present end-to-end simulation, we use the CME generation mechanism described in the “Simulation of Solar Eruptions” section and run the simulation all the way from the solar surface to beyond 1 AU. We used up to 14 million computational cells with AMR. The smallest cell size was 1/32 solar radii (21,750 km), while the largest cell size was 4 solar radii (2.785×10^6 km). We carried out the grid refinement so that the CME evolution along the Sun–Earth line was well resolved, while far away from this line the grid remained relatively coarse.

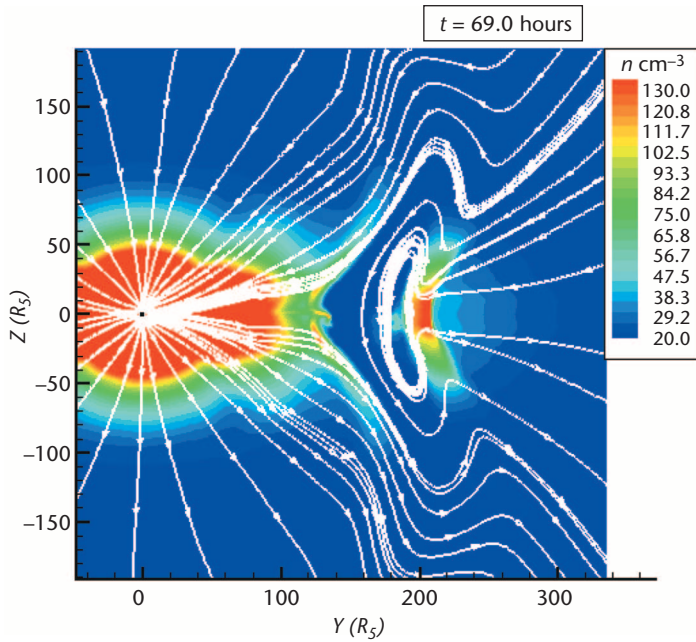


Figure 14. Meridional cut through the coronal mass ejection as it approaches Earth at around 69 hours after the initiation. The color code represents the solar-wind plasma density, while the white lines represent the projection of magnetic field lines onto the meridional plane.

This method enabled us to have good spatial and time resolution in simulating the interaction of the CME with the magnetosphere, while still employing a manageable total number of computational cells.

Figure 14 shows a 2D cut through the CME in the meridional plane going through the expanding magnetic flux-rope. White lines represent magnetic streamlines in the meridional plane, while the color code shows the plasma density. An accumulation of material behind the leading shock and in front of the leading edge of the propagating flux rope is called the snowplow effect. You can see the magnetic closed-loop structure of the flux rope surrounded by open field lines of the solar wind and a significantly depleted density structure inside the magnetic flux rope that drives the CME.

The resolution along the Sun–Earth axis near the leading edge of the CME (near the location of Earth) is $1/8$ solar radii (approximately 14 Earth radii). This resolution is unprecedented in Sun–Earth simulations, and it enables us to achieve approximately 4-minute temporal resolution in describing the interaction between the CME structure and the magnetosphere–ionosphere system.

Figure 15 shows the temporal evolution of the solar-wind parameters just upstream of Earth as the CME moves by. From top to bottom, the panels show the three components of the magnetic

field vector and the solar-wind density and radial velocity, respectively. We initiated the CME on 21 March, 2000 at 1210 UT. The first signature of the CME arrived about 69 hours later in the form of the shock. Note that the solar wind radial velocity jumps by about 100 km/s when the CME arrives and that efficient application of AMR makes the shock’s leading edge very well resolved. The solar-wind velocity remains nearly constant throughout the density pile-up preceding the magnetic bubble structure associated with the expanding flux rope. When Earth enters the magnetic bubble at around 80 hours after event initiation, the velocity exhibits a slow decrease while the density suddenly drops nearly an order of magnitude. At this time the B_z component of the interplanetary magnetic field exhibits its most important variation from the point of view of geo-effective interaction: first it increases to about +20 nT (northward IMF) and then it rotates to -20 nT (southward IMF) in about three hours. This rotation is highly geo-effective and it generates all kinds of geomagnetic activities, such as reconfiguration of magnetospheric topology.

Figure 16 illustrates the geo-effectiveness of the B_z rotation. The four panels represent noon–midnight meridional cuts through the 3D magnetosphere solutions at 1800, 1900, 2000, and 2100 UT. The peak of the northward IMF is at 1800 UT with $B_z \approx 20$ nT. At 1900 UT, the B_z still is northward (≈ 10 nT), and it changes sign shortly before 2000 UT. At 2000 UT, the B_z already is southward, and the magnetosphere exhibits a transitional state. The magnetosphere shows day side reconnection characterizing southward IMF conditions, while at the same time the long magnetotail looks very much like a northward IMF configuration. Clearly, the effect of the IMF southward turning had not yet propagated all the way down the magnetotail. The last panel shows a snapshot at 2100 UT, well over an hour after the IMF turned south at the nose of the magnetosphere. At this time, the magnetosphere shows a fundamentally southward configuration, but the complex and long tail is a clear indicator that the configuration is still changing and this is far from equilibrium.

The ionospheric convection pattern also dramatically changes during the IMF southward turning. The cross-polar cap potential changes from 75 kV at 1800 UT to 190 kV at 2100 UT, consistent with the reconfiguration of the magnetosphere.

This simulation is the first successful attempt to use first-principles-based global simulation codes to launch and follow a CME near the Sun and describe its highly geo-effective interaction with the

terrestrial magnetosphere. We are confident that researchers will routinely carry out similar space-weather simulations in the future and use the results to forecast space-weather events.

Space-plasma simulations greatly matured in the last decade. New simulation codes employ modern and efficient numerical methods and are able to run much faster than real time on parallel computers. Our simulation capabilities also are rapidly evolving. In the next few years, model coupling will be at the center of development. A few years from now we will be able to simulate the individual elements of the complex Sun–Earth system with the help of a software framework that automatically takes care of the coupling of various components. Our goal is to accomplish validated predictive capabilities of space-weather events and hazards.

Acknowledgments

US Department of Defense Multidisciplinary University Research Initiative grant F49620-01-1-0359, National Science Foundation Knowledge and Distributed Intelligence grant NSF ATM-9980078, NSF Computer and Information for Science and Engineering grant ACI-9876943, NASA Earth Science and Technology Office/Computational Technologies Cooperative Agreement NCC5-614, and NASA Applied Information Systems Research Program grant NAG5-9406 at the University of Michigan supported research for this manuscript. The Hungarian Science Foundation (OTKA grant T037548) partially supported Gábor Tóth.

References

1. B. van Leer, "Towards the Ultimate Conservative Difference Scheme V. A Second-Order Sequel to Godunov's Method," *J. Computational Physics*, vol. 32, no. 1, 1979, pp. 101–136.
2. C.R. Evans and J.F. Hawley, "Simulation of Magnetohydrodynamic Flows: A Constrained Transport Method," *Astrophysical J.*, vol. 332, 1988, pp. 659–677.
3. K.G. Powell, *An Approximate Riemann Solver for Magnetohydrodynamics (That Works in More than One Dimension)*, tech. report 94-24, Inst. for Computer Applications in Science and Eng., NASA Langley Space Flight Center, 1994.
4. P.D. Lax and B. Wendroff, "Systems of Conservation Laws," *Comm. Pure and Applied Mathematics*, vol. 13, 1960, pp. 217–237.
5. S.K. Godunov, "Symmetric Form of the Equations of Magnetohydrodynamics," *Numerical Methods for Mechanics of Continuum Medium*, Siberian Branch of USSR Academy of Science, vol. 1, 1972, pp. 26–34 (in Russian).
6. T.I. Gombosi et al., "Semi-Relativistic Magnetohydrodynamics and Physics-Based Convergence Acceleration," *J. Computational Physics*, vol. 177, 2002, pp. 176–205.
7. J.P. Boris, *A Physically Motivated Solution of the Alfvén Problem*, tech. report, NRL Memorandum Report 2167, Naval Research Lab., 1970.

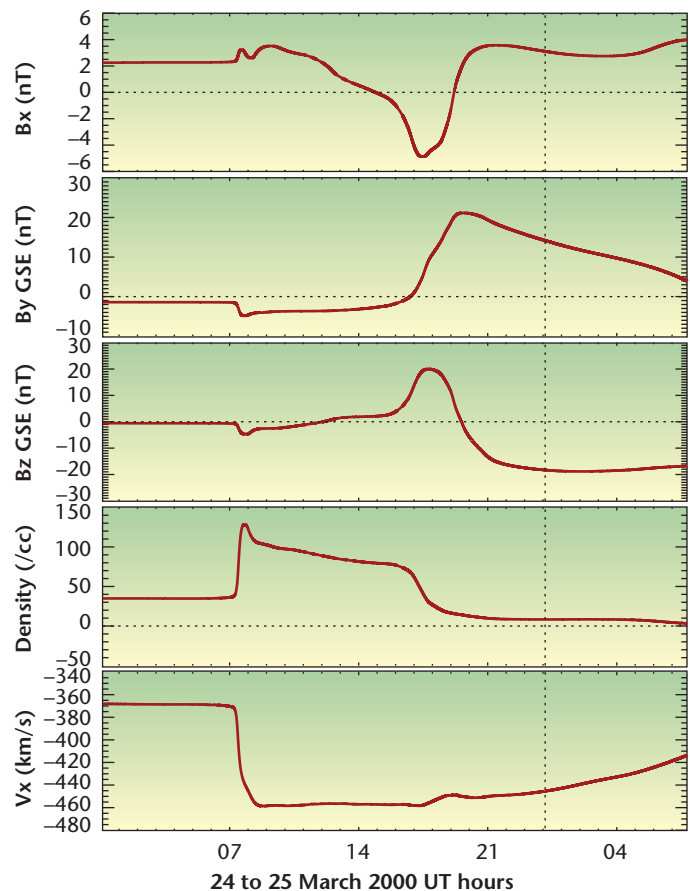


Figure 15. Temporal evolution of the solar-wind parameters just upstream of Earth as the CME moves by. The panels show the three components of the magnetic field vector, the solar wind density and speed, respectively. The CME was initiated on March 21, 2000 at 1210 UT.

8. S.K. Godunov, "A Difference Scheme for Numerical Computation of Discontinuous Solutions of Hydrodynamic Equations," *Sbornik: Math.*, vol. 47, no. 3, 1959, pp. 271–306 (in Russian).
9. P.L. Roe, "Approximate Riemann Solvers, Parameter Vectors, and Difference Schemes," *J. Computational Physics*, vol. 43, 1981, pp. 357–372.
10. B. van Leer, "Towards the Ultimate Conservative Difference Scheme. II. Monotonicity and Conservation Combined in a Second-Order Scheme," *J. Computational Physics*, vol. 14, 1974, pp. 361–370.
11. G. Tóth, "The $\nabla \cdot \mathbf{B}$ Constraint in Shock Capturing Magnetohydrodynamic Codes," *J. Computational Physics*, vol. 161, 2000, pp. 605–652.
12. K.G. Powell et al., "A Solution-Adaptive Upwind Scheme for Ideal Magnetohydrodynamics," *J. Computational Physics*, vol. 154, no. 2, 1999, pp. 284–309.
13. J.U. Brackbill and D.C. Barnes, "The Effect of Nonzero $\nabla \cdot \mathbf{B}$ on the Numerical Solution of the Magnetohydrodynamic Equations," *J. Computational Physics*, vol. 35, 1980, pp. 426–430.
14. G. Tóth and P.L. Roe, "Divergence- and Curl-Preserving Prolongation Formulas," *J. Computational Physics*, vol. 180, 2002, pp. 736–750.
15. D.L. De Zeeuw and K.G. Powell, "An Adaptively-Refined Cartesian Mesh Solver for the Euler Equations," *J. Computational Physics*, vol. 104, 1993, pp. 55–68.

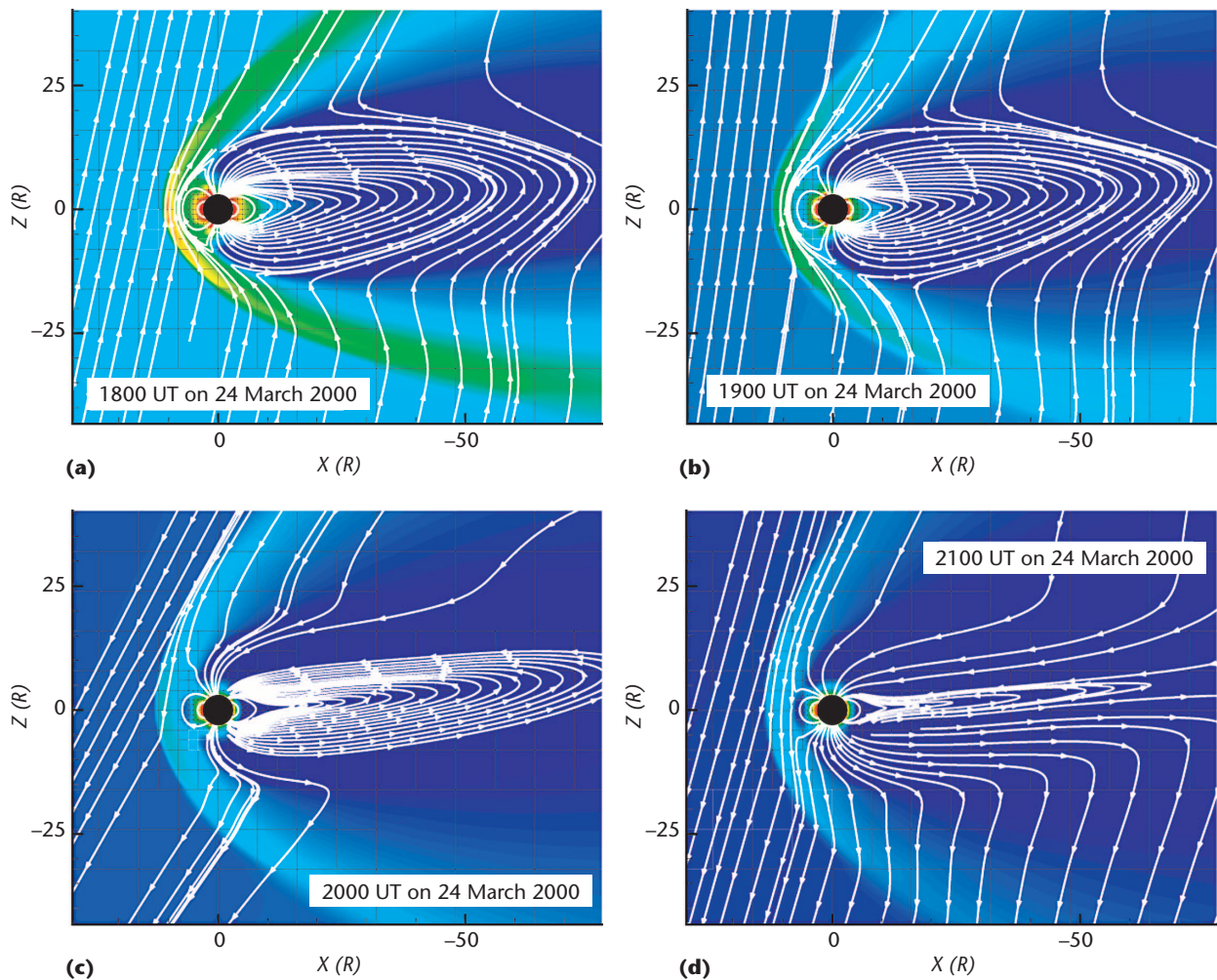


Figure 16. Noon–midnight meridional cuts through the 3D magnetosphere solutions at (a) 1800, (b) 1900, (c) 2000, and (d) 2100 UT. The peak of the northward interplanetary magnetic field is at 1800 UT with $B_z \approx 20$ nT. The color code represents pressure, while the white lines are projections of the magnetic field lines to the meridional plane.

16. T. J. Linde, *A Three-Dimensional Adaptive Multifluid MHD Model of the Heliosphere*, doctoral thesis, Dept. of Aerospace Engineering, Univ. of Mich., 1998.
17. I. Sokolov et al., "Artificial Wind—A New Framework to Construct Simple and Efficient Upwind Shock-Capturing Schemes," *J. Computational Physics*, vol. 181, 2002, pp. 354–393.
18. C.P.T. Groth et al., "Global 3D MHD Simulation of a Space Weather Event: CME Formation, Interplanetary Propagation, and Interaction with the Magnetosphere," *J. Geophysical Research*, vol. 105, 2000, pp. 25053–25078.
19. T.I. Gombosi et al., "The Length of the Magnetotail for Northward IMF: Results of 3D MHD Simulations," *Physics of Space Plasmas*, T. Chang and J.R. Jasperse, eds., vol. 15, 1998, pp. 121–128.
20. P. Song et al., "A Numerical Study of Solar Wind–Magnetosphere Interaction for Northward IMF," *J. Geophysical Research*, vol. 104, 1999, pp. 28361–28378.
21. T.J. Linde et al., "The Heliosphere in the Magnetized Local Interstellar Medium: Results of a 3D MHD Simulation," *J. Geophysical Research*, vol. 103, 1998, pp. 1889–1904.
22. T.I. Gombosi et al., "Three-dimensional Multiscale MHD Model of Cometary Plasma Environments," *J. Geophysical Research*, vol. 101, 1996, pp. 15233–15253.
23. R.M. Häberli et al., "Modeling of Cometary X-Rays Caused by Solar Wind Minor Ions," *Science*, vol. 276, 1997, pp. 939–942.
24. K. Kabin et al., "Interaction of Mercury with the Solar Wind," *Icarus*, vol. 143, 2000, pp. 397–406.
25. R. Bauske et al., "A Three-Dimensional MHD Study of Solar Wind Mass Loading Processes at Venus: Effects of Photoionization, Electron Impact Ionization, and Charge Exchange," *J. Geophysical Research*, vol. 103, 1998, pp. 23625–23638.
26. Y. Liu et al., "3D Multi-Fluid MHD Studies of the Solar Wind Interaction with Mars," *Geophysical Research Letters*, vol. 26, 1999, pp. 2689–2692.
27. K.C. Hansen et al., "A 3D Global MHD Simulation of Saturn's Magnetosphere," *Advances Space Research*, vol. 26, 2000, pp. 1681–1690.
28. K. Kabin et al., "Interaction of the Saturnian Magnetosphere with Titan: Results of a 3D MHD Simulation," *J. Geophysical Research*, vol. 104, 1999, pp. 2451–2458.
29. K. Kabin et al., "Io's Magnetospheric Interaction: an MHD Model with Day-Night Asymmetry," *Planetary Space Science*, vol. 49, 2001, pp. 337–344.
30. I.I. Roussev et al., "A Three-Dimensional Flux Rope Model for Coronal Mass Ejections Based on a Loss of Equilibrium," *Astro-*

physical J., vol. 588, 2003, pp. L45–L48.

31. V.S. Titov and P. Démoulin, "Basic Topology of Twisted Magnetic Configurations in Solar Flares," *Astronomy and Astrophysics*, vol. 351, 1999, pp. 701–720.
32. W.B. Manchester et al., "Three-Dimensional MHD Simulation of a Flux-Rope Driven CME," doi:10.1029/2002JA009672, *J. Geophysical Research*, vol. 109, 2004, pp. A01102.
33. S. Gibson and B.C. Low, "A Time-Dependent Three-Dimensional Magnetohydrodynamic Model of the Coronal Mass Ejection," *Astrophysical J.*, vol. 493, 1998, pp. 460–473.

Tamas I. Gombosi is professor and chair of the Department of Atmospheric, Oceanic, and Space Sciences at the University of Michigan. His research interests include space-plasma physics, planetary science, and space weather. He has an MSc and PhD from the Lóránd Eötvös University, Budapest, Hungary. He is a fellow of the American Geophysical Union and a member of the International Academy of Astronautics, the American Physical Society, and the American Astronomical Society. Contact him at tamas@umich.edu.

Kenneth G. Powell is professor of aerospace engineering at the University of Michigan. His research interests include computational space physics and computational aerodynamics. He has an ScD from MIT. He is an associate fellow of the American Institute of Aeronautics and Astronautics. Contact him at powell@umich.edu.

Darren L. De Zeeuw is an associate research scientist in the Department of Atmospheric, Oceanic, and Space Sciences at the University of Michigan. His research interests include space-plasma physics, space weather, and large research code development. He has a BSc from Calvin College and an MSc and a PhD from the University of Michigan. He is a member of the American Geophysical Union and a senior member of the American Institute of Aeronautics and Astronautics. Contact him at darrens@umich.edu.

C. Robert Clauer is research professor and co-director of the Center for Space Environment Modeling within the Department of Atmospheric, Oceanic, and Space Sciences at the University of Michigan. His research interests include solar wind–magnetosphere–ionosphere coupling, magnetospheric electrodynamics, space weather, and computer networks in support of scientific activities. He has an MSc and a PhD from the University of California, Los Angeles. He is a member of the American Geophysical Union. Contact him at rclauer@umich.edu.

Kenneth C. Hansen is an assistant research scientist at the University of Michigan. His research interests include magnetospheric science and the plasma environment of comets, Jupiter, and Saturn. He has a BSc and an MSc from Brigham Young University and a PhD from the University of Michigan. He is a member of the American

Geophysical Union. Contact him at kenhan@umich.edu.

Ward B. Manchester is an assistant research scientist in the Department of Atmospheric, Oceanic, and Space Sciences at the University of Michigan. His research interests include solar and heliospheric physics with an emphasis on coronal mass ejections and magnetic flux emergence. He has an MSc and a PhD from the University of Illinois. He is a member of the American Astronomical Society and the American Geophysical Union. Contact him at chipm@umich.edu.

Aaron J. Ridley is an associate research scientist at the University of Michigan. His research interests include ionospheric and thermospheric physics, ionosphere-magnetosphere coupling, and data assimilation. He has an MSc and a PhD from the University of Michigan. He is a member of the American Geophysical Union. Contact him at ridley@umich.edu.

Iliia Roussev is an assistant research scientist at the Department of Atmospheric, Oceanic, and Space Sciences at the University of Michigan. His research interests include solar and heliospheric physics, space-plasma physics, and space weather. He has an MSc from Sofia University, Sofia, Bulgaria, and a PhD from Queen's University, Belfast, Northern Ireland. He is a member of the American Geophysical Union and the American Astronomical Society. Contact him at irussev@umich.edu.

Igor V. Sokolov is an associate research scientist at the University of Michigan. His research interests include computational, plasma, and laser physics. He has a PhD from the General Physics Institute of Russian Academy of Sciences, Moscow. He is a member of the American Physical Society and the American Geophysical Society. Contact him at igorsok@umich.edu.

Quentin F. Stout is professor of electrical engineering and computer science, and co-director of the Center for Space Environment Modeling, at the University of Michigan. His research interests include parallel and scientific computing, adaptive statistical designs, and algorithms. He has a BA from Centre College and a PhD in mathematics from Indiana University. Contact him at qstout@umich.edu.

Gábor Tóth is an associate research scientist at the University of Michigan and an associate professor at Eötvös University, Budapest, Hungary. His research interests include computational magnetohydrodynamics and its applications in space physics and astrophysics. He has a PhD in the astrophysical sciences from Princeton University. He is a member of the American Geophysical Union. Contact him at gtoth@umich.edu.